Advanced Composites and Hybrid Materials (2022) 5:2977–2987
https://doi.org/10.1007/s42114-022-00524-0

ORIGINAL RESEARCH

Synthesis of $CoSe_2$/Mxene composites using as high-performance anode materials for lithium-ion batteries

Zihao Yan[1] · Jianbao Li[1] · Qing Chen[1] · Shuaifeng Chen[1] · Lijie Luo[1] · Yongjun Chen[1]

Received: 19 April 2022 / Revised: 17 May 2022 / Accepted: 19 June 2022 / Published online: 30 August 2022

Abstract

Currently, the energy densities of commercial lithium-ion batteries (LIBs) are getting closer and closer to their fundamental limit, and novel anode materials are urgent to be explored to meet the increasing requirements. $CoSe_2$ has a high theoretical specific capacity of 494.4 mAh g^{-1} and is expected to be a viable anode material for high-power LIBs. However, its actual specific capacity degrades rapidly during the cycling process, while the MXene $Ti_3C_2T_x$ possesses excellent cycle stability but low specific capacity (about 110 mAh g^{-1}). In this study, novel $CoSe_2/Ti_3C_2T_x$ composites with high specific capacity and good stability were successfully prepared by growing $CoSe_2$ particles in situ on $Ti_3C_2T_x$ via hydrothermal method. The results showed that after 1000 charge–discharge cycles at a current density of 0.3 A g^{-1}, $CoSe_2/Ti_3C_2T_x$ (with a molar ratio of 1:2) composite still has a high reversible capacity of 210.8 mAh g^{-1}. Excellent rate capability and electrochemical kinetic behavior are also achieved. This study indicates that $CoSe_2/Ti_3C_2T_x$ composites have a promising application prospect in LIBs as an anode material.

Keywords $CoSe_2$ · $Ti_3C_2T_x$ · Mxene · Anode material · Lithium-ion battery

1 Introduction

Today, with the exhaustion of fossil energy represented by petroleum and the increasing serious environmental pollution, there is an urgent demand for sustainable renewable energies [1–7]. Moreover, the advances in technology also require smaller and lighter devices with high power [8] such as supercapacitors (SC) and lithium-ion batteries (LIBs) [9–13]. LIBs play important roles in electronic devices because of their high energy density, long cycle life, and environmental friendliness. But the performances of LIBs such as theoretical capacity, charge–discharge voltage, and cycle stability are affected by the inherent characteristics of electrode materials dramatically [3, 14, 15]. At present, some materials including carbon-based materials [16], silicon-based materials [17], niobium-based materials ($Mo_3Nb_{14}O_{44}$ and $V_3Nb_{17}O_{50}$) [18, 19], and vanadium-based materials ($Na_2Ca(VO_3)_4$ and VPO_5) [20, 21] are popularly used as anode materials for LIBs. Graphite, the commonly used commercial anode material, only has a theoretical capacity of 372 mAh g^{-1} [22, 23]. Therefore, seeking novel anode materials with higher specific capacity, higher charge–discharge rate, and cycle stability is necessary to meet future market demands [24].

Transition metal selenides are attracting more and more attentions because of their conversion reaction mechanism [25–29] and relatively high storage capacity of lithium. Among them, $CoSe_2$ has been paid special attention due to the rich content of Co and its low price, high specific capacity, and safety [30–33]. However, $CoSe_2$ suffers from a large volume change during the charge–discharge process that leads to the rapid decay of specific capacity and poor cycle stability. Therefore, researchers developed several strategies to overcome the poor cycle stability problem of Co_xSe_y by preparing Co_xSe_y microspheres or nanosheets, or coating Co_xSe_y with carbon material and introducing carbon base [34–41]. However, their cycle stabilities are still not satisfactory.

It is reported that the design of multilayer templates for anode materials could provide more active sites, which is conducive to the higher specific capacity [42, 43]. Therefore, two-dimensional (2D) materials have been widely explored

✉ Lijie Luo
luolijie4567@163.com

✉ Yongjun Chen
chenyjtg@163.com

[1] School of Materials Science and Engineering, State Key Laboratory of Marine Resource Utilization in South China Sea, Hainan University, Haikou 570228, China

and used in many fields [44–49]. MXenes, discovered in 2011 [50], are a relatively new member of 2D material family, including a class of transition metal carbonitrides. The 2D layer-structured MXenes are of great interest and are considered as the most promising energy storage material because of their unique physical and chemical properties, such as metal conductivity, hydrophilic surface, large and adjustable layer spacing, and excellent mechanical properties [51–53]. MXenes have a general formula $M_{n+1}X_nT_x$, where M is transition metal (e.g. Ti, Mo, V, Nb, and Ta), X represents C or N, and T is surface functional group (e.g. OH, F, Cl, or O) that are formed by violent reactions of transition metals with water or fluoride ions [54–56]. Up to now, more than 40 MXenes have been synthesized successfully [57], which are applied in the fields of energy storage [58], electromagnetic shielding [59, 60], catalysis [61], and sensors [62]. Among them, $Ti_3C_2T_x$ is one of the most studied MXene, exhibiting excellent cycle stability and higher theoretical lithium ion storage capacity (up to 447.8 mAh g^{-1}) [63–66].

Therefore, novel $CoSe_2/Ti_3C_2T_x$ composite with high specific capacity and excellent cycle stability can be expected if the advantages of both $CoSe_2$ and $Ti_3C_2T_x$ are combined. In this study, $Ti_3C_2T_x$ was firstly prepared by hydrofluoric acid corrosion method, and then $CoSe_2$ particles were grown on $Ti_3C_2T_x$ via hydrothermal method. $Ti_3C_2T_x$, as a buffer layer of volume change, could effectively alleviate the volume change and aggregation of $CoSe_2$ particles by the formation of strong Ti-Se-Co bonds. Meanwhile, $Ti_3C_2T_x$ could provide more relevant electronic channels in the composite. The fabricated $CoSe_2/Ti_3C_2T_x$ composites were found to possess excellent electrochemical performances.

2 Experimental

2.1 Material synthesis

Firstly, 2 g of Ti_3AlC_2 (98%, Shanghai Macklin Biochemical Co., Ltd.) was slowly added to 20 ml of 40% HF acid solution, which was stirred at room temperature for 24 h. After centrifugation of the above solution at 5000 rpm for 10 min, the supernatant was poured out. Deionized water was added to the precipitation left in the centrifuge tube, which was shaken by hand to mix the precipitation and deionized water evenly, followed by centrifugation for several times to remove the HF solution. Then, the liquid was pumped, filtered, and vacuum dried to get $Ti_3C_2T_x$ powder. After that, suitable amount of $Ti_3C_2T_x$ powder, $Co(NO_3)_2{\cdot}6H_2O$ (98.5%, Xilong Scientific Co., Ltd.), Se powder (analytically pure, Tianjin Kemiou Chemical Reagent Co., Ltd.) were mixed in an ethanol aqueous solution and stirred for 1 h. The molar ratios of $CoSe_2/Ti_3C_2T_x$ were designed to be 1:2.5, 1:2, 1:1.5, and the resulted $CoSe_2/Ti_3C_2T_x$ composites were denoted by sample CT1, CT2, and CT3, respectively. The solution was then poured into a hydrothermal autoclave that was held at 200 °C for 16 h. After being cooled to room temperature naturally, the solution was taken out, filtered with suction, and vacuum dried for 2 h. The $CoSe_2/Ti_3C_2T_x$ composites were finally prepared. Figure 1 illustrates the typical preparation process of $CoSe_2/Ti_3C_2T_x$ composite.

2.2 Material characterization

The raw materials used and prepared composites were characterized by X-ray powder diffractometer (XRD, D8-Advance, Germany), scanning electron microscopy (SEM, S4800, Japan), Brunauer-Emmet-Teller method (BET, ASAP 2460, USA), transmission electron microscopy (TEM, FEI Talos F200X, USA) equipped with energy-dispersive X-ray spectrometer (EDS), and X-ray photoelectron spectroscopy (XPS, Thermo Escalab 250Xi, USA).

2.3 Half-cell measurement

The electrochemical properties of $CoSe_2/Ti_3C_2T_x$ composites (CT1-CT3) were tested by assembling them into 2016 coin cells. Firstly, 80 wt% $CoSe_2/Ti_3C_2T_x$ composite (acting as active material), 10 wt% conductive carbon black, and 10 wt% polyvinylidene fluoride (PVDF, adhesive) were mixed. N-Methylpyrrolidone (NMP) was then added and stirred for 12 h to form a slurry. The slurry was coated onto a copper foil, which was dried in a vacuum drying oven at 120 °C for 12 h. After that, the copper foil loaded with active material was cut into

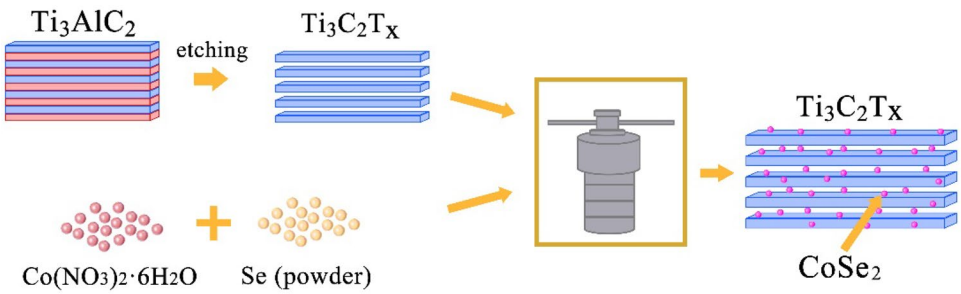

Fig. 1 The sketch diagram for the typical preparation process of $CoSe_2/Ti_3C_2T_x$ composite

circular electrodes with a diameter of 10 mm. Argon (99.99%)-filled glove box ($O_2 < 0.1$ ppm, $H_2O < 0.1$ ppm) was employed to assemble the coin cells. Lithium sheets were used as reference electrodes, and polyethylene/polypropylene film (PE/PP, Celgard 2325) was applied as the separator. A commercial electrolyte with 1 M $LiPF_6$ dissolved in a mixture of ethyl carbonate, diethyl carbonate, and dimethyl carbonate (1:1:1 by volume) was used. Constant current charge–discharge test was performed on a battery performance tester (Neware CT-4000, China). Cyclic voltammetry (CV) and electrochemical impedance spectroscopy (EIS) measurements were conducted by an electrochemical workstation (Zahner Zronach, Germany). All electrochemical tests were performed at a constant temperature of 25 °C.

3 Results and discussion

Figure 2 shows the XRD patterns of the raw material of Ti_3AlC_2 powder, synthesized $Ti_3C_2T_x$ powder, and $CoSe_2$/$Ti_3C_2T_x$ composite (CT2). It can be seen that after etching, (104) diffraction peak of Ti_3AlC_2 phase (JCPDS # 52–0875) disappears, indicating that Ti_3AlC_2 phase is successfully changed into $Ti_3C_2T_x$ phase [67, 68]. Moreover, the (002) peak shifts from 9.7 to 7.1°, hinting that the layer spacing increases in $Ti_3C_2T_x$ phase. From the XRD patterns of CT2, it can be seen that $CoSe_2$ phase (JCPDS # 53–0449) appears obviously in addition to the original $Ti_3C_2T_x$ phase, which reveals the formation of $CoSe_2/Ti_3C_2T_x$ composite.

Figure 3 demonstrates the SEM images of $Ti_3C_2T_x$, CT1, CT2, and CT3. It can be seen that $Ti_3C_2T_x$ exhibits an accordion-like structure (Fig. 3a), indicating that the Al layer in Ti_3AlC_2 has been removed. Figure 3b–d illustrate that $CoSe_2$ particles are successfully grown on the surface of $Ti_3C_2T_x$ after hydrothermal reaction. But only in CT2 there are an appropriate amount of $CoSe_2$ particles in the $Ti_3C_2T_x$ substrate (Fig. 3c), while few $CoSe_2$ particles are formed in CT1 (Fig. 3b) and too much $CoSe_2$ particles with an accumulation nature are formed in CT3 (Fig. 3d).

Figure 4 shows the N_2 adsorption/desorption isotherms of CT1-CT3. The BET-specific areas of CT1-CT3 are calculated to be 19.13, 23.04, and 29.15 $m^2\ g^{-1}$, respectively. It can be seen that the specific surface area increases with the

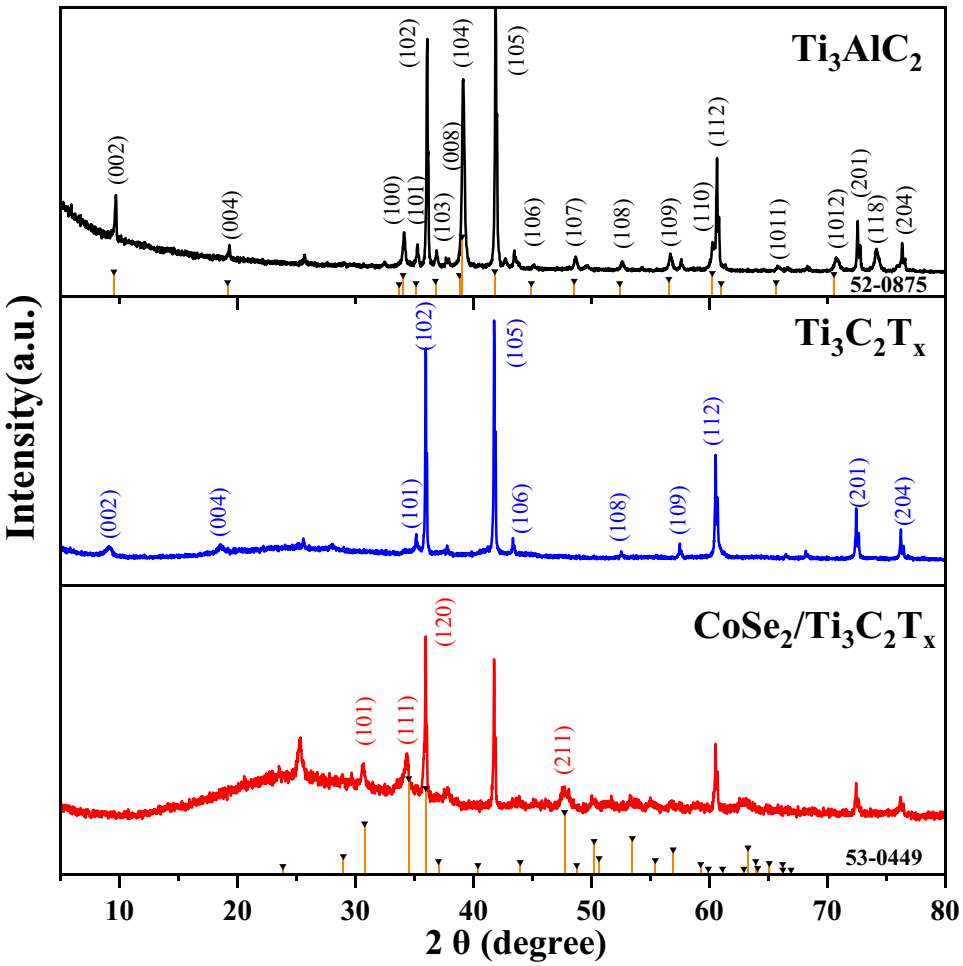

Fig. 2 XRD patterns of Ti_3AlC_2, $Ti_3C_2T_x$, and CT2

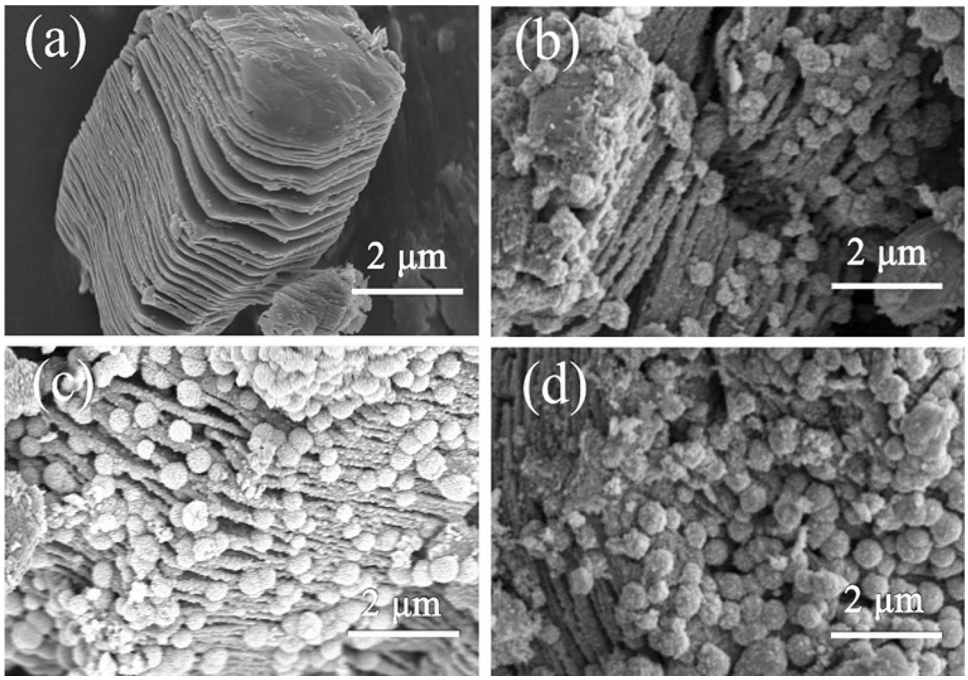

Fig. 3 SEM images of samples **a** $Ti_3C_2T_x$, **b** CT1, **c** CT2, and **d** CT3

rise of $CoSe_2$ content added. Large specific surface area of the $CoSe_2/Ti_3C_2T_x$ composite is believed to favor the provision of more active sites that facilitates the storage of lithium ions [69, 70].

In order to further study the structural characteristics of $CoSe_2/Ti_3C_2T_x$ composite, TEM characterization was carried out on sample CT2 and the results are shown in Fig. 5. $CoSe_2$ particles grown evenly on the surface of $Ti_3C_2T_x$ substrate can also be observed (Fig. 5a), and the average size of $CoSe_2$ particles is about 240 nm (Fig. 5b). As shown in the corresponding high-resolution TEM (HRTEM) image (Fig. 5c), the lattice spacing between two neighboring fringes is estimated to be 0.928 nm, which corresponds to the (002) planes of $Ti_3C_2T_x$. The lattice spacing between two neighboring fringes of a $CoSe_2$ particle are measured to be 0.190, 0.249, and 0.259 nm, which correspond to the (211), (120), and (111) planes of $CoSe_2$, respectively (Fig. 5d). The elemental mapping images shown in Fig. 5e–i demonstrate the uniform distribution of C, Ti, Co, and Se elements, further revealing the successful preparation of $CoSe_2/Ti_3C_2T_x$ composite.

The interaction between $CoSe_2$ particles and $Ti_3C_2T_x$ was studied by XPS. Figure 6a shows the Ti 2P spectra of $Ti_3C_2T_x$ (top) and CT2 (bottom). The peak at 455.1 eV corresponds to Ti-C bond. In addition, two peaks are observed at 455.8 and 457.2 eV, which can be attributed to Ti^{2+} and Ti^{3+}, respectively [71, 72]. Ti^{4+} also appears at 458.9 eV due to the surface oxidation of $Ti_3C_2T_x$ during the preparation process [73]. The Co 2p spectra of $CoSe_2$ (top) and CT2 (bottom) are illustrated in Fig. 6b. The two peaks located at 778.6 eV and 781.1 eV can be ascribed to Co^{3+} and Co^{2+}, respectively [74]. Figure 6c shows the Se 3d spectra of $CoSe_2$ (top) and CT2 (bottom), and the peak at 54.9 eV is attributed to Se^{2-}. In Fig. 6a, the Ti^{2+} and Ti^{3+} peaks of $Ti_3C_2T_x$ almost disappear after the formation of $CoSe_2/Ti_3C_2T_x$ composite, and the signal of Ti^{4+} peak is greatly enhanced. While the Co^{2+} peak of $CoSe_2/Ti_3C_2T_x$ composite gets stronger in comparison with that of $CoSe_2$ (Fig. 6b). The valency of Se does not change significantly (Fig. 6c). Moreover, it can be found from Fig. 6a, b that electron transfer occurs between Ti and Co, Ti is connected with Se then with Co, and finally Ti-Se-Co bonds are formed.

Figure 7a–c demonstrate the first four cycle CV curves of $Ti_3C_2T_x$, $CoSe_2$, and CT2 at 0.2 mV s^{-1}, respectively. An irreversible reduction peak appears in the first cycle, which can be attributed to the generation of SEI layer. However, this peak disappears in the subsequent cycles, hinting that a stable SEI layer is already formed after the first cycle. The curves of the second, third, and fourth cycles almost overlap (Fig. 7a). The reduction peak at ~1.134 V may be due to the chemical reaction between $Ti_3C_2T_x$ and Li^+, while the oxidation peak at ~0.876 V can be ascribed to the generation of $Ti_3C_2Li_x$. In the first CV cycle of $CoSe_2$ (Fig. 7b), the reduction peaks at about ~0.506 and ~1.138 V probably refer to the conversion of $CoSe_2$ to Co metal and Li_2Se, respectively. In addition, strong oxidation peaks at ~2.103 and ~1.126 V appear due to the formation of $CoSe_2$ by the reaction between Co and Li_2Se. The lithium storage mechanism of $CoSe_2$ can be described by a two-stage reversible reaction: $CoSe_2 + Li^+ + e^- \leftrightharpoons Li_xCoSe_2$ and $Li_xCoSe_2 + e^- \leftrightharpoons Co + Li_2Se$ [75]. Moreover, compared with those in the first circle, the two reaction peaks

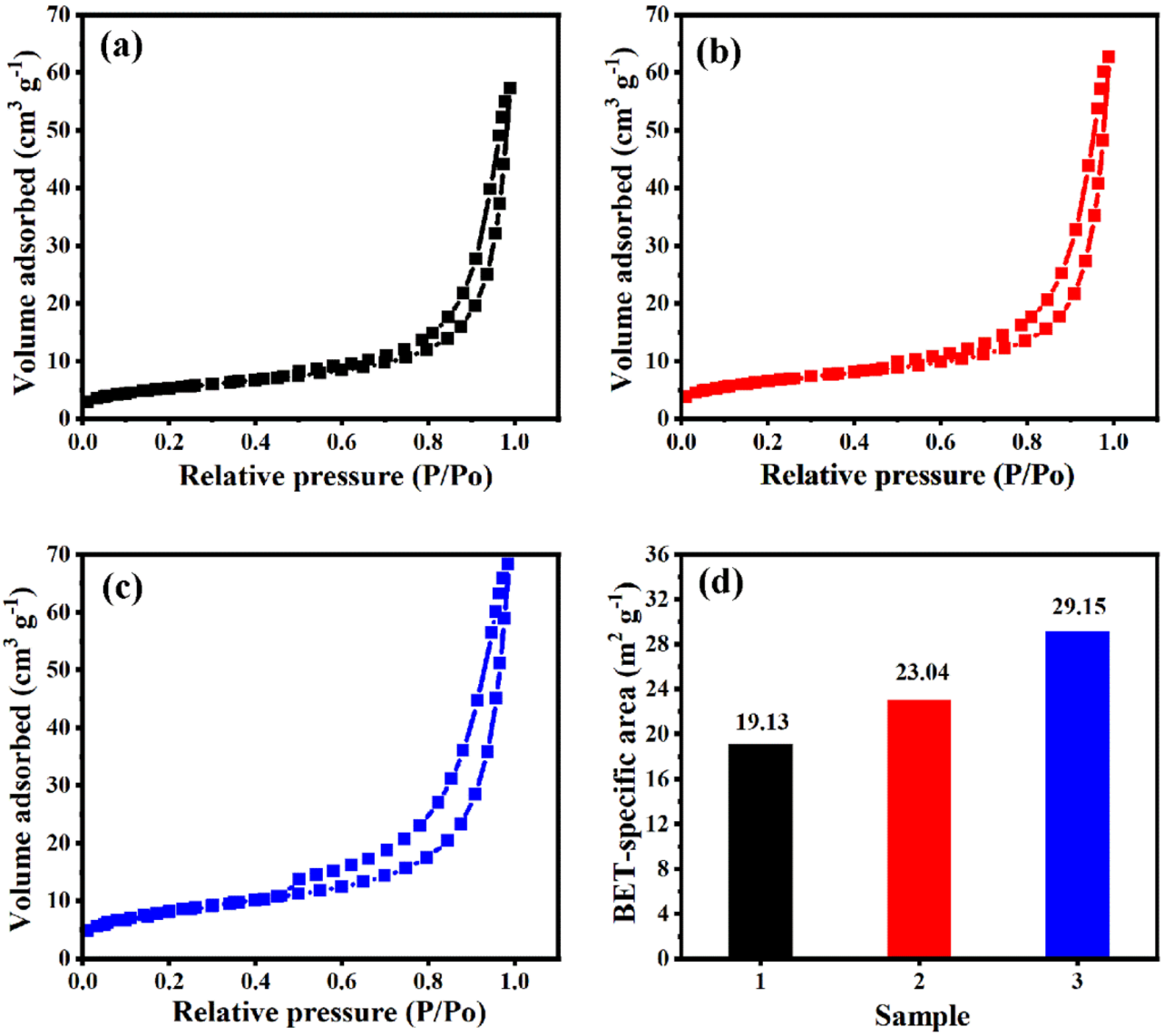

Fig. 4 Nitrogen adsorption/desorption isotherms of **a** CT1, **b** CT2, and **c** CT3. The BET-specific areas of **d** CT1-CT3

at ~ 0.506 and ~ 1.138 V in the second circle shift to ~0.653 and ~1.394 V, respectively, which may be caused by the formation of SEI layer, decomposition of electrolyte, and microstructure change.

The electric potentials of the reduction peak and oxidation peak in the third and fourth cycles are similar to those in the second cycle, but the response current decreases significantly, hinting a poor reversibility of $CoSe_2$ during the lithium-delithium process caused by the large volume change and comminution effect of $CoSe_2$ electrode. The CV curve of CT2 is an approximate combination of $CoSe_2$ and $Ti_3C_2T_x$ CV curve, indicating an improvement of the reversibility in comparison with that of $CoSe_2$, as is shown in Fig. 7c. And the curves in the second, third, and fourth cycles of CT2 almost overlap because $Ti_3C_2T_x$ buffers the volume expansion of $CoSe_2$ particles and the formation of Ti-Se-Co bond could prevent $CoSe_2$ from dissolving into the electrolyte.

Figure 7d illustrates the CV curves of CT2 at scanning rates of 0.4, 0.6, 0.8, and 1.0 mV s^{-1}. It can be observed that the redox potential difference does not change significantly with the increase of scanning rate, revealing an excellent rate capability and small electrode polarization of CT2. Figure 7e–g show the charge–discharge curves of $Ti_3C_2T_x$, $CoSe_2$, and CT2 in the first three cycles at 0.1 A g^{-1}, respectively, indicating the lower Coulombic efficiencies of $Ti_3C_2T_x$ (52.39%), $CoSe_2$ (55.03%), and CT2 (69.24%) that are caused by the irreversible redox reactions.

Figure 8a demonstrates the rate performance of $Ti_3C_2T_x$, $CoSe_2$, and CT2-made electrodes at current densities of

0.03, 0.06, 0.15, 0.3, and 0.6 A g^{-1} after 10 cycles. When the current density returns from 0.6 A g^{-1} to the initial 0.03 A g^{-1}, the specific capacities of $Ti_3C_2T_x$ and CT2 nearly do not decay, revealing their good reversibilities. But the specific capacity of $CoSe_2$ increases, indicating that $CoSe_2$ electrode underwent more activation than other samples. In addition, it can be seen that as the current density increases, the specific capacities of all samples decrease gradually. That is because at high rates, a large number of electrolyte ions will be adsorbed on the interface between electrode and electrolyte, resulting in a rapid decrease of the concentration of electrolyte ions and thereby enhancing the concentration polarization, but the polarization voltage does not contribute

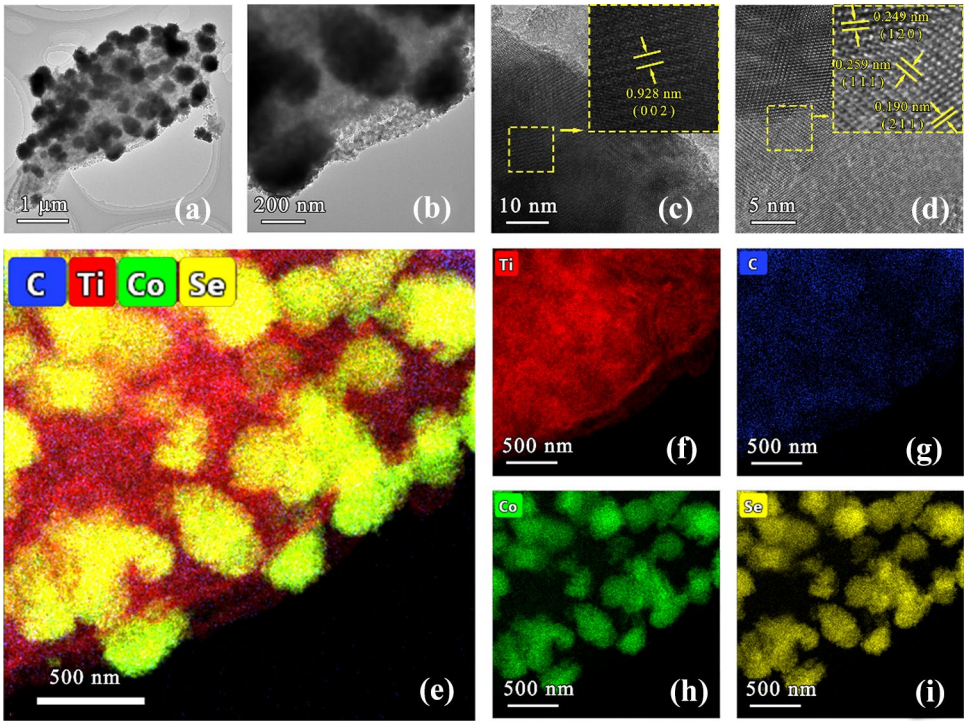

Fig. 5 Low-magnification (**a**) and high-magnification (**b**) TEM images of CT2. HRTEM images of the part of $Ti_3C_2T_x$ (**c**) and part of a $CoSe_2$ particle (**d**). The corresponding elemental mapping images (**e–i**)

Fig. 7 CV curves of **a** $Ti_3C_2T_x$, **b** $CoSe_2$, and **c** CT2 at 0.2 mV s^{-1} in the first four cycles. **d** CV curves of CT2 at different rates. Charge–discharge curves of the first three cycles of **e** $Ti_3C_2T_x$, **f** $CoSe_2$, and **g** CT2

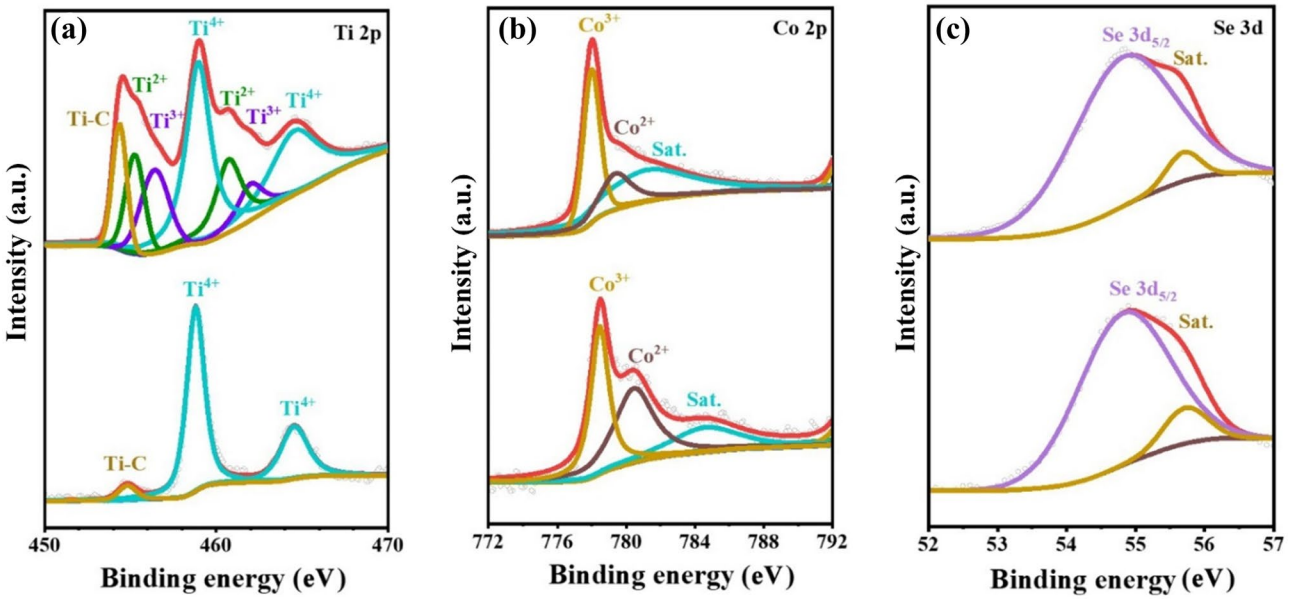

Fig. 6 XPS spectra of **a** Ti 2p, **b** Co 2p, and **c** Se 3d in $Ti_3C_2T_x$ and CT2

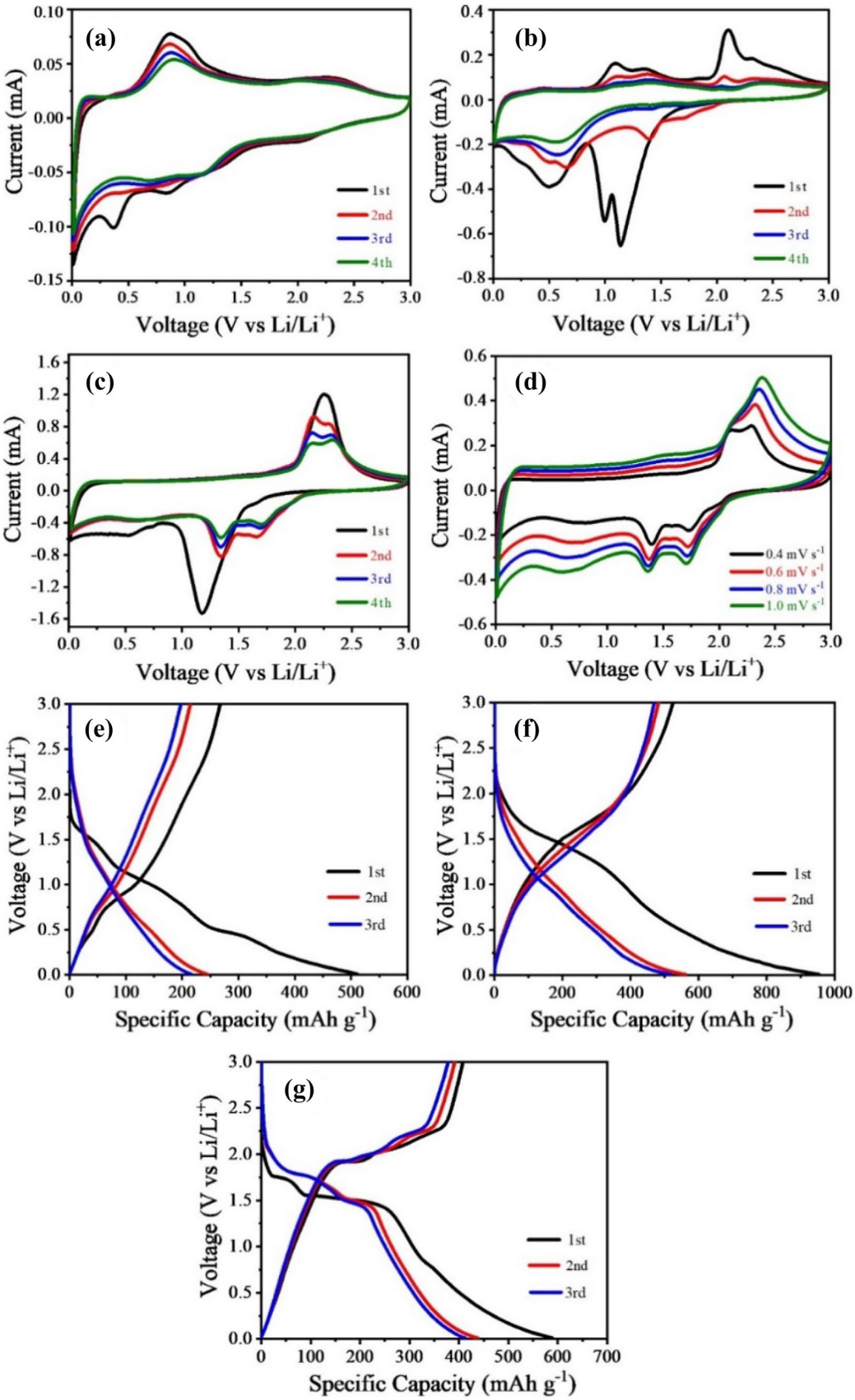
(a)
Current (mA)
Voltage (V vs Li/Li+)
1st
2nd
3rd
4th
(b)
Current (mA)
Voltage (V vs Li/Li+)
1st
2nd
3rd
4th
(c)
Current (mA)
Voltage (V vs Li/Li+)
1st
2nd
3rd
4th
(d)
Current (mA)
Voltage (V vs Li/Li+)
0.4 mV s-1
0.6 mV s-1
0.8 mV s-1
1.0 mV s-1
(e)
Voltage (V vs Li/Li+)
Specific Capacity (mAh g-1)
1st
2nd
3rd
(f)
Voltage (V vs Li/Li+)
Specific Capacity (mAh g-1)
1st
2nd
3rd
(g)
Voltage (V vs Li/Li+)
Specific Capacity (mAh g-1)
1st
2nd
3rd

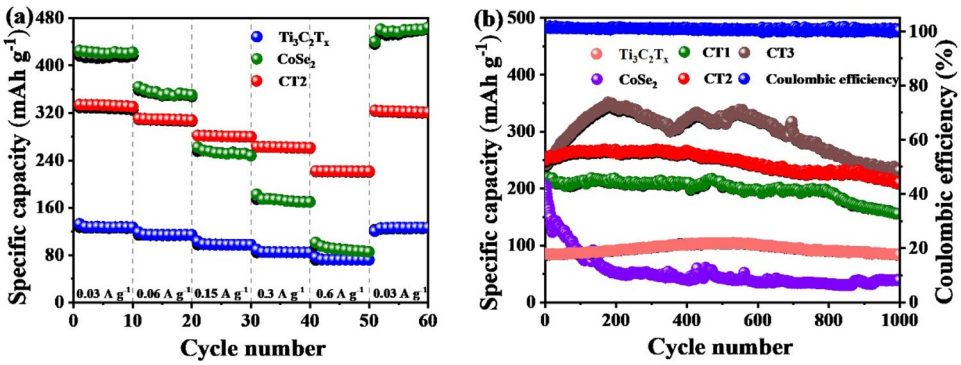

Fig. 8 **a** Rate performance of $Ti_3C_2T_x$, $CoSe_2$, and CT2. **b** Cycling stability of $Ti_3C_2T_x$, $CoSe_2$, CT1, CT2, and CT3 at 0.3 A g^{-1} for 1000 cycles and the Coulombic efficiency of CT2

any specific capacity. The rate performance of $CoSe_2$ is poor, while $Ti_3C_2T_x$ exhibits excellent rate performance. Thus, by combining $Ti_3C_2T_x$ with $CoSe_2$, the $CoSe_2/Ti_3C_2T_x$ composite (CT2) displays high electronic conductivity and excellent performance at high current density. Moreover, CT2 has the best rate performance because of its smaller polarization during redox process. The specific capacities of CT2 at current densities of 0.03, 0.06, 0.15, 0.3, and 0.6 A g^{-1} are 331.95, 310.90, 280.47, 262.22, and 220.79 mAh g^{-1}, respectively.

Figure 8b shows the cyclic stability of $Ti_3C_2T_x$, $CoSe_2$, CT1, CT2, and CT3 after 1000 cycles at a current density of 0.3 A g^{-1}. It can be seen obviously that the cyclic stabilities of CT1-CT3 are higher than those of $CoSe_2$ but lower than that of $Ti_3C_2T_x$. And after 1000 cycles, the specific capacities of $Ti_3C_2T_x$, $CoSe_2$, CT1, CT2, and CT3 are 84.06, 39.09, 156.10, 210.80, and 232.01 mAh g^{-1}, respectively. These results indicate that $Ti_3C_2T_x$ can only load a certain amount of $CoSe_2$ particles, and excessive $CoSe_2$ particles will aggregate and undergo large volume change and comminution effect during the charge–discharge process, which may result in the formation of new surfaces and reactivation and finally the enhancement of specific capacity. However, $CoSe_2$ may dissolve into the electrolyte later, causing a significant reduction of specific capacity. In addition, the excellent lithium storage performances of CT1-CT3 can be attributed to the stable layered structure of $Ti_3C_2T_x$ which provides additional active sites and improves the electronic conductivity. The formation of Ti-Se-Co bonds between $Ti_3C_2T_x$ and $CoSe_2$ particles also helps to alleviate the volume change of $CoSe_2$ during the cycling process.

Figure 9 shows the microscopic topography of CT2 after 1000 cycles at a current density of 0.3 A g^{-1}. It can be seen that the sample as a whole still keeps a lamellar structure, indicating a good structural stability of the composite. In addition, the $CoSe_2$ particle number seems to decrease, which may be caused by the dissolution of $CoSe_2$ particles during the cycling process.

Electrochemical impedance spectroscopy (EIS) reveals the electrochemical behavior of $Ti_3C_2T_x$, $CoSe_2$, and CT2 samples, as is illustrated in Fig. 10. A typical EIS curve consists of a straight line representing the low-frequency region of the interfacial charge transfer impedance and a semicircular line representing the mid-frequency region of the lithium diffusion impedance [68]. Impedance data are

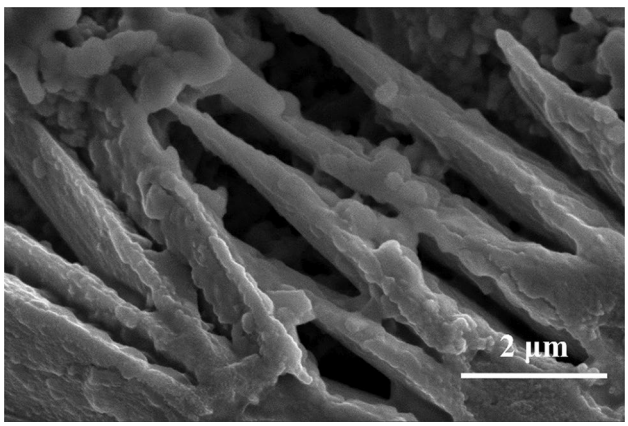

Fig. 9 SEM images of CT2 after 1000 cycles

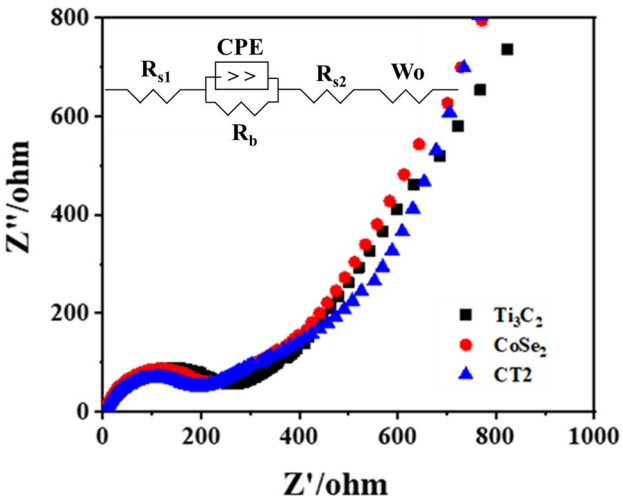

Fig. 10 Nyquist plots of $Ti_3C_2T_x$, $CoSe_2$, and CT2

Table 1 The comparison of electrochemical properties between the CT2 and those related materials reported

Materials	Specific capacity (mAh g^{-1})	Current density (A g^{-1})	Cycle number	References
CoSe/NC	310.11	0.1	500	[34]
CoSe@PCP	675	0.2	100	[35]
CoSe/Co@NC	640	1	500	[36]
$CoSe_2$ nanoparticles	143	0.25	300	[37]
$CoSe_2$@N-PGC/CNTs	492	0.2	100	[38]
CoSe/C–NS nanocubes	1494	0.2	300	[39]
$Co_{0.85}Se$ microspheres	170	0.2	50	[40]
$Co_{0.85}Se$ nanosheets	516	0.2	50	[40]
$Co_{0.85}Se$@C/$Ti_3C_2T_x$	700	0.1	270	[41]
MA-Ti_3C_2	200	0.1	150	[77]
Ti_3C_2@TiO_2	154	2	1500	[78]
$CoSe_2$/$Ti_3C_2T_x$	210.80	0.3	1000	this work

described by an equivalent circuit fit in the inset. The circuit consists of electrolyte resistance (Rs1), charge transfer resistance (Rs2), constant phase element (CPE), and Warburg impedance (Zw) [76]. Obviously, the semicircle diameter of CT2 is smaller than those of $CoSe_2$ and $Ti_3C_2T_x$; therefore, CT2 can provide more active sites and reduce its resistance, which benefit the electron transfer.

The electrochemical properties of CT2 are compared with those of other $Ti_3C_2T_x$- and Co_xSe_y-based anodes reported, as are listed in Table 1. It can be seen that CT2 possesses higher specific capacity than several $Ti_3C_2T_x$-based anodes and higher stability than several Co_xSe_y anodes. It is believed that the reactive anode material of $CoSe_2$ mainly contributes to the higher specific capacity of CT2, and the layered structure of CT2 also favors the improvement of specific capacity. On the other hand, the formation of Ti-Se-Co bonds between $Ti_3C_2T_x$ and $CoSe_2$ leads to a better structural stability. Therefore, the excellent cyclical stability of $Ti_3C_2T_x$ and high specific capacity of $CoSe_2$ enable CT2 to exhibit excellent electrochemical performances.

4 Conclusions

In summary, novel $CoSe_2$/$Ti_3C_2T_x$ composites are successfully prepared with high specific capacity and excellent cycling stability. After 1000 cycles at 0.3 A g^{-1}, a high specific capacity of 210.80 mAh g^{-1} is achieved. The introduction of $Ti_3C_2T_x$ is believed to ease the volume expansion of $CoSe_2$ during charge–discharge cycles, resulting in the improvement of cycling stability. Moreover, the excellent electronic conductivity of $Ti_3C_2T_x$ favors the electrochemical behavior of $CoSe_2$/$Ti_3C_2T_x$ composites. Therefore, $CoSe_2$/$Ti_3C_2T_x$ composites with high specific capacity and excellent cycling stability are achieved, which may find promising applications in LIBs as anode materials.

Funding The work is supported by the Natural Science Foundation of Hainan Province (No. 518MS021) and High Level Talents Project of Basic and Applied Basic Research Plan of Hainan Province (in Natural Science) (No. 2019RC029).

Declarations

Conflict of interest The authors declare no competing interests.

References

1. Ding FC, Hu H, Ding H, Li JJ, Chen Y, Xiao M, Meng YZ, Sun LY (2020) Sulfonated poly(fluorene ether ketone) (SPFEK)/α-zirconium phosphate (ZrP) nanocomposite membranes for fuel cell applications. Adv Compos Hybrid Mater 3:546–550
2. Zeng XY, Luo Q, Li JY, Li YL, Wang W, Li YH, Wu RG, Pan D, Song G, Li JB, Guo ZH, Wang N (2021) A multifunctional pentlandite counter electrode toward efficient and stable sensitized solar cells. Adv Compos Hybrid Mater 4:392–400
3. Xiao LD, Qi HJ, Qu KQ, Shi C, Cheng Y, Sun Z, Yuan BN, Huang ZH, Pan D, Guo ZH (2021) Layer-by-layer assembled free-standing and flexible nanocellulose/porous Co_3O_4 polyhedron hybrid film as supercapacitor electrodes. Adv Compos Hybrid Mater 4:306–316
4. Ali Baig AB, Rathinam V, Ramya V (2021) Facile fabrication of Zn-doped SnO_2 nanoparticles for enhanced photocatalytic dye degradation performance under visible light exposure. Adv Compos Hybrid Mater 4:114–126
5. Hu H, Ding FC, Ding H, Liu JJ, Xiao M, Meng YZ, Sun LY (2020) Sulfonated poly (fluorenyl ether ketone)/sulfonated α-zirconium phosphate nanocomposite membranes for proton exchange membrane fuel cells. Adv Compos Hybrid Mater 3:498–507
6. Jain B, Hashmi A, Sanwaria S, Singh AK, Susan MABH, Singh A (2020) Zinc oxide nanoparticle incorporated on graphene oxide: an efficient and stable photocatalyst for water treatment through the Fenton process. Adv Compos Hybrid Mater 3:231–242
7. Babu MJ, Botsa SM, Rani SJ, Venkateswararao B, Muralikrishna R (2020) Enhanced photocatalytic degradation of cationic dyes under visible light irradiation by $CuWO_4$-RGO nanocomposite. Adv Compos Hybrid Mater 3:205–212
8. Melchior SA, Palaniyandy N, Sigalas I, Iyuke SE, Ozoemena KI (2019) Probing the electrochemistry of MXene (Ti_2CT_x)/

electrolytic manganese dioxide (EMD) composites as anode materials for lithium-ion batteries. Electrochim Acta 297:961–973
9. Hou CX, Wang B, Murugadoss V, Vupputuri S, Chao YF, Guo ZH, Wang CY, Du W (2020) Recent advances in Co_3O_4 as anode materials for high-performance lithium-ion batteries. Eng Sci 11:19–30
10. Wang YZ, Liu YX, Wang C, Liu H, Zhang JX, Lin J, Fan JC, Ding T, Guo RGE, ZH, (2020) Significantly enhanced ultrathin NiCo-based MOF nanosheet electrodes hybrided with $Ti_3C_2T_x$ MXene for high performance asymmetric supercapacitor. Eng Sci 9:50–59
11. Ma YP, Xie XB, Yang WY, Yu ZP, Sun XQ, Zhang YP, Yang XY, Kimura H, Hou CX, Guo ZH, Du W (2021) Recent advances in transition metal oxides with different dimensions as electrodes for high-performance supercapacitors. Adv Compos Hybrid Mater 4:906–924
12. Rehman SU, Ahmed R, Ma K, Xu S, Tao TX, Aslam MA, Amir M, Wang JF (2020) Composite of strip-shaped ZIF-67 with polypyrrole: a conductive polymer-MOF electrode system for stable and high specific capacitance. Eng Sci 13:71–78
13. Patil SS, Bhat TS, Teli AM, Beknalkar SA, Dhavale SB, Faras MM, Karanjkar MM, Patil PS (2020) Hybrid solid state supercapacitors (HSSC's) for high energy & power density: an overview. Eng Sci 12:38–51
14. Eames C, Islam MS (2014) Ion intercalation into two-dimensional transition-metal carbides: global screening for new high-capacity battery materials. J Am Chem Soc 136:16270–16276
15. Xie J, Lu YC (2020) A retrospective on lithium-ion batteries. Nat Commun 11:2499
16. Li L, Zhang D, Deng JP, Gou YC, Fang JF, Cui H, Zhao YQ, Cao MH (2021) Carbon-based materials for fast charging lithium-ion batteries. Carbon 183:721–734
17. Zhang YX, Wu B, Mu G, Ma CW, Mu DB, Wu F (2022) Recent progress and perspectives on silicon anode: synthesis and prelithiation for LIBs energy storage. J Energy Chem 64:615–650
18. Li RJ, Liang GS, Zhu XZ, Fu QF, Chen YJ, Luo LJ, Lin CF (2021) $Mo_3Nb_{14}O_{44}$: a new Li^+ container for high-performance electrochemical energy storage. Energy Environ Mater 4:65–71
19. Fu QF, Zhu XZ, Li RJ, Liang GS, Luo LJ, Chen YJ, Ding YL, Lin CH, Wang KK, Zhao XS (2020) A low-strain $V_3Nb_{17}O_{50}$ anode compound for superior Li^+ storage. Energy Stor Mater 30:401–411
20. Yang LT, Liang GS, Cao HJ, Ma SY, Liu XH, Li X, Chen GY, You WB, Lin CF, Che RC (2022) A new sodium calcium cyclotetravanadate framework: "zero-strain" during large-capacity lithium intercalation. Adv Funct Mater 32:2105026
21. Ma SY, Jiang T, Deng JB, Zhang Q, Ou YJ, Liu XH, Lin CF, Wang KK, Zhao XS (2022) VPO_5: an all-climate lithium-storage material. Energy Stor Mater 46:366–373
22. Long ZW, Yuan LH, Shi C, Wu CQ, Qiao H, Wang KL (2022) Porous Fe_2O_3 nanorod-decorated hollow carbon nanofibers for high-rate lithium storage. Adv Compos Hybrid Mater 5:370–382
23. Lv CP, Lin CH, Zhao XS (2021) Rational design and synthesis of nickel niobium oxide with high-rate capability and cycling stability in a wide temperature range. Adv Energy Mater 12:2102550
24. Huang JP, Chen Q, Chen SH, Luo LJ, Li JB, Lin CH, Chen YJ (2021) Al^{3+}-doped $FeNb_{11}O_{29}$ anode materials with enhanced lithium-storage performance. Adv Compos Hybrid Mater 4:733–742
25. Yang J, Gao HC, Men S, Shi ZQ, Lin Z, Kang XW, Chen SW (2018) $CoSe_2$ nanoparticles encapsulated by n-doped carbon framework intertwined with carbon nanotubes:high-performance dual-role anode materials for both li- and na-ion batteries. Adv Sci 5:1800763
26. Zhou JD, Lin JH, Huang XW, Zhou Y, Chen Y, Xia J, Wang H, Xie Y, Yu HM, Lei JC, Wu D, Liu FC, Fu QD, Zeng QS, Hsu CH, Yang CL, Lu L, Yu T, Shen ZX, Lin H, Yakobson BI, Liu Q, Suenaga K, Liu GT, Liu Z (2018) A library of atomically thin metal chalcogenides. Nature 556:355–359
27. Zhang SP, Wang G, Jin J, Zhang LL, Wen ZY, Yang JH (2018) Robust and conductive red $MoSe_2$ for stable and fast lithium storage. ACS Nano 12:4010–4018
28. Yang L, Hong WW, Tian Y, Zou GQ, Hou HS, Sun W, Ji XB (2020) Heteroatom-doped carbon inlaid with Sb_2X_3 (X= S, Se) nanodots for high-performance potassium-ion batteries. Chem Eng J 385:123838
29. Etogo CA, Huang HW, Hong H, Liu GX, Zhang L (2020) Metal-organic-frameworks-engaged formation of $Co_{0.85}Se$@C nanoboxes embedded in carbon nanofibers film for enhanced potassium-ion storage. Energy Storage Mater 24:167–176
30. Zhang K, Park MH, Zhou LM, Lee GH, Li WJ, Kang YM, Chen J (2016) Urchin-like $CoSe_2$ as a high-performance anode material for sodium-ion batteries. Adv Funct Mater 26:6728–6735
31. Yu QY, Jiang B, Hu J, Lao CY, Gao YZ, Li PH, Liu ZW, Suo GQ, He DL, Wang W, Yin GP (2018) Metallic octahedral $CoSe_2$ threaded by N-doped carbon nanotubes:a flexible framework for high-performance potassium-ion batteries. Adv Sci 5:1800782
32. Yin H, Qu HQ, Liu ZT, Jiang RZ, Li C, Zhu MQ (2019) Long cycle life and high rate capability of three dimensional $CoSe_2$ grain-attached carbon nanofibers for flexible sodium-ion batteries. Nano Energy 58:715–723
33. Zhao S, Jin RX, Abroshan H, Zeng CJ, Zhang H, House SD, Gottlieb E, Kim HJ, Yang JC, Jin RC (2017) Gold nanoclusters promote electrocatalytic water oxidation at the nanocluster/$CoSe_2$ interface. J Am Chem Soc 139:1077–1080
34. Li ZY, Zhang LY, Zhang L, Huang JM, Liu HD (2019) ZIF-67-derived CoSe/NC composites as anode materials for lithium-ion batteries. Nanoscale Res Lett 14:358
35. Li JB, Yan D, Lu T, Yao YF, Pan LK (2017) An advanced CoSe embedded within porous carbon polyhedra hybrid for high performance lithium-ion and sodium-ion batteries. Chem Eng J 325:14–24
36. Zhou Y, Tian R, Duan H, Wang KF, Guo YP, Li H, Liu HZ (2018) CoSe/Co nanoparticles wrapped by in situ grown N-doped graphitic carbon nanosheets as anode material for advanced lithium ion batteries. J Power Sources 399:223–230
37. Lu WZ, Xue MZ, Chen XL, Chen C (2017) $CoSe_2$ nanoparticlesas anode for lithium ion battery. Int J Electrochem Sci 12:1118–1129
38. Park SK, Kim JK, Kang YC (2017) Excellent sodium-ion storage performances of $CoSe_2$ nanoparticles embedded within N-doped porous graphitic carbon nanocube/carbon nanotube composite. Chem Eng J 328:546–555
39. Cui LF, Qi HY, Wang NN, Gao X, Song CY, Yang JH, Wang G, Kang SF, Chen XD (2022) N/S co-doped CoSe/C nanocubes as anode materials for Li-ion batteries. Nanotechnol Rev 11:244–251
40. Zhou JS, Wang Y, Zhang J, Chen TP, Song HH, Yang HY (2016) Two dimensional layered $Co_{0.85}Se$ nanosheets as a high-capacity anode for lithium-ion batteries. Nanoscale 8:14992–15000
41. Ding W, Wang S, Wu XZ, Wang YS, Li YY, Zhou PF, Zhuo T, Zhuo J, Zhuo SP (2020) $Co_{0.85}Se$@C/$Ti_3C_2T_x$ MXene hybrids as anode materials for lithium-ion batteries. J Alloys Compd 816:152566
42. Pomerantseva E, Bonaccorso F, Feng XL, Cui Y, Gogotsi Y (2019) Energy storage: the future enabled by nanomaterials. Science 366:8285
43. Li RJ, Lin CF, Wang N, Luo LJ, Chen YJ, Li JB, Guo ZH (2018) Advanced composites of complex Ti-based oxides as anode materials for lithium-ion batteries. Adv Compos Hybrid Mater 1:440–459
44. Sun JF, Mu Q, Kimura H, Murugadoss V, He MX, Du W, Hou CX (2022) Oxidative degradation of phenols and substituted phenols in the water and atmosphere: a review. Adv Compos Hybrid Mater
45. Wu XH, Chen ZX, Wu F (2021) Strong nonreciprocal radiation in a InAs film by critical coupling with a dielectric grating. ES Energy Environ 13:8–12

46. Li J, Tang XG, Liu QX, Jiang YP, Li WH (2021) Enhancement of the photoelectric properties of composite oxide TiO_2-$SrTiO_3$ thin films. Adv Compos Hybrid Mater
47. Cheng HR, Pan YM, Chen Q, Che RC, Zheng GQ, Liu CT, Shen CY, Liu XH (2021) Ultrathin flexible poly (vinylidene fluoride)/MXene/silver nanowire film with outstanding specific EMI shielding and high heat dissipation. Adv Compos Hybrid Mater 4:505–513
48. Yan H, Dai XJ, Ruan KP, Zhang SJ, Shi XT, Guo YQ, Cai HQ, Gu JW (2021) Flexible thermally conductive and electrically insulating silicone rubber composite films with BNNS@Al_2O_3 fillers. Adv Compos Hybrid Mater 4:36–50
49. Mishra S, Chaudhary P, Yadav BC, Umar A, Lohia P, Dwivedi DK (2021) Fabrication and characterization of an ultrasensitive humidity sensor based on chalcogenide glassy alloy thin films. Eng Sci 15:138–147
50. Naguib M, Kurtoglu M, Presser V, Lu J, Niu JJ, Heon M, Hultman L, Gogotsi Y, Barsoum MW (2011) Two-dimensional nanocrystals produced by exfoliation of Ti_3AlC_2. Adv Mater 23:4248–4253
51. Anasori B, Lukatskaya MR, Gogotsi Y (2017) 2D metal carbides and nitrides (MXenes) for energy storage. Nat Rev Mater 2:16098
52. Pu LY, Zhang JX, Jiresse NKL, Gao YF, Zhou HJ, Naik N, Gao P, Guo ZH (2022) N-doped MXene derived from chitosan for the highly effective electrochemical properties as supercapacitor. Adv Compos Hybrid Mater 5:356–369
53. Nan JX, Guo X, Xiao J, Li X, Chen WH, Wu WJ, Liu H, Wang Y, Wu MH, Wang GX (2021) Nanoengineering of 2D MXene-based materials for energy storage applications. Small 17:1902085
54. Chen NJ, Yang WQ, Zhang CF (2021) Perspectives on preparation of two-dimensional MXenes. Sci Technol Adv Mater 22:917–930
55. Guo Y, Wang DD, Bai TT, Liu H, Zheng YJ, Liu CT, Shen CY (2021) Electrostatic self-assembled $NiFe_2O_4$/$Ti_3C_2T_x$ MXene nanocomposites for efficient electromagnetic wave absorption at ultralow loading level. Adv Compos Hybrid Mater 4:602–613
56. Srivastava P, Mishra A, Mizuseki H, Lee KR, Singh AK (2016) Mechanistic insight into the chemical exfoliation and functionalization of Ti_3C_2 MXene. ACS Appl Mater Interfaces 8:24256–24264
57. Firouzjaei MD, Karimiziarani M, Moradkhani H, Elliott M, Anasori B (2022) MXenes: the two-dimensional influencers. Mater Today Adv 13:100202
58. Gogotsi Y, Anasori B (2019) The rise of MXenes. ACS Nano 13:8491–8494
59. Iqbal A, Shahzad F, Hantanasirisakul K, Kim MK, Kwon J, Hong J, Kim D, Gogotsi Y, Koo CM (2020) Anomalous absorption of electromagnetic waves by 2D transition metal carbonitride Ti_3CNT_x (MXene). Science 369:446–450
60. Gao QS, Pan YM, Zheng GQ, Liu CT, Shen CY, Liu XH (2021) Flexible multilayered MXene/thermoplastic polyurethane films with excellent electromagnetic interference shielding, thermal conductivity, and management performances. Adv Compos Hybrid Mater 4:274–285
61. Zhang K, Li DQ, Cao HY, Zhu QH, Trapalis C, Zhu PF, Gao XH, Wang CY (2021) Insights into different dimensional MXenes for photocatalysis. Chem Eng J 424:130340
62. Pei YY, Zhang XL, Hui ZY, Zhou JY, Huang X, Sun GZ, Huang W (2021) $Ti_3C_2T_X$ MXene for sensing applications: recent progress, design principles, and future perspectives. ACS Nano 15:3996–4017
63. Tian Y, An YL, Feng JK (2019) Flexible and freestanding silicon/MXene composite papers for high-performance lithium-ion batteries. ACS Appl Mater Interfaces 11:10004–10011
64. Zhong SL, Ju SL, Shao YF, Chen W, Zhang TF, Huang YQ, Zhang HY, Xia GL, Yu XB (2021) Magnesium hydride nanoparticles anchored on MXene sheets as high capacity anode for lithium-ion batteries. J Energy Chem 62:431–439
65. Wei YD, Luo WL, Zhuang Z, Dai B, Ding JX, Li TX, Ma ML, Yin XQ, Ma Y (2021) Fabrication of ternary MXene/MnO_2/polyaniline nanostructure with good electrochemical performances. Adv Compos Hybrid Mater 4:1082–1091
66. Er D, Li JW, Naguib M, Gogotsi Y, Shenoy VB (2014) Ti_3C_2 MXene as a high capacity electrode material for metal (Li, Na, K, Ca) ion batteries. ACS Appl Mater Interfaces 6:11173–11179
67. Fan YP, Chen DD, Liu XY, Fan GX, Liu BZ (2019) Improving the hydrogen storage performance of lithium borohydride by Ti_3C_2 MXene. Int J Hydrogen Energy 44:29297–29303
68. Luo JM, Tao XY, Zhang J, Xia Y, Huang H, Zhang LY, Gan YP, Liang C, Zhang WK (2016) Sn^{4+} ion decorated highly conductive Ti_3C_2 MXene: promising lithium-ion anodes with enhanced volumetric capacity and cyclic performance. ACS Nano 10:2491–2499
69. Wu NN, Zhao BB, Liu JY, Li YL, Chen YB, Chen L, Wang M, Guo ZH (2021) MOF-derived porous hollow Ni/C composites with optimized impedance matching as lightweight microwave absorption materials. Adv Compos Hybrid Mater 4:707–715
70. Zhai YJ, Yang WY, Xie XB, Sun XQ, Wang J, Yang XY, Naik N, Kimura H, Du W, Guo ZH, Hou CX (2022) Co_3O_4 nanoparticle-dotted hierarchical-assembled carbon nanosheet framework catalysts with the formation/decomposition mechanisms of Li_2O_2 for smart lithium-oxygen batteries. Inorg Chem Front 9:1115–1124
71. Yan J, Ren CE, Maleski K, Hatter CB, Anasori B, Urbankowski P, Gogotsi Y (2017) Flexible MXene/graphene films for ultrafast supercapacitors with outstanding volumetric capacitance. Adv Funct Mater 27:1701264
72. Lu CX, Li AR, Li GZ, Yan Y, Zhang MY, Yang QL, Zhou W, Guo L (2021) S-decorated porous Ti_3C_2 MXene combined with In situ forming Cu_2Se as effective shuttling interrupter in Na-Se batteries. Adv Mater 33:2008414
73. Ahmed B, Anjum DH, Hedhili MN, Gogotsi Y, Alshareef HN (2016) H_2O_2 assisted room temperature oxidation of Ti_2C MXene for Li-ion battery anodes. Nanoscale 8:7580–7587
74. Yuan H, Jiao QZ, Liu J, Liu XF, Li YJ, Shi DX, Wu Q, Zhao Y, Li HS (2017) Facile synthesis of $Co_{0.85}Se$ nanotubes/reduced graphene oxide nanocomposite as Pt-free counter electrode with enhanced electrocatalytic performance in dye-sensitized solar cells. Carbon 122:381–388
75. Zhang GJ, Liu KH, Liu ST, Song HH, Zhou JS (2018) Flexible $Co_{0.85}Se$ nanosheets/graphene composite film as binder-free anode with high Li- and Na-Ion storage performance. J Alloys Compd 731:714–722
76. Zhang LJ, Xia GL, Guo ZP, Li XG, Sun DL, Yu XB (2016) Boron and nitrogen co-doped porous carbon nanotubes webs as a high-performance anode material for lithium ion batteries. Int J Hydrogen Energy 41:14252–14260
77. Liu MC, Zhang BM, Zhang YS, Hu YX (2021) Diacid molecules welding achieved self-adaption layered structure Ti_3C_2 MXene toward fast and stable lithium-ion storage. ACS Sustainable Chem Eng 9:12930–12939
78. Li L, Jiang GX, An CH, Xie ZJ, Wang YJ, Jiao LF, Yuan HT (2020) Hierarchical Ti_3C_2@TiO_2 MXene hybrids with tunable interlayer distance for highly durable lithium-ion batteries. Nanoscale 12:10369–10379